🔓 **Open Access**

Effect of Scalp Hair Follicles on NIRS Quantification by Monte Carlo Simulation and Visible Chinese Human Dataset
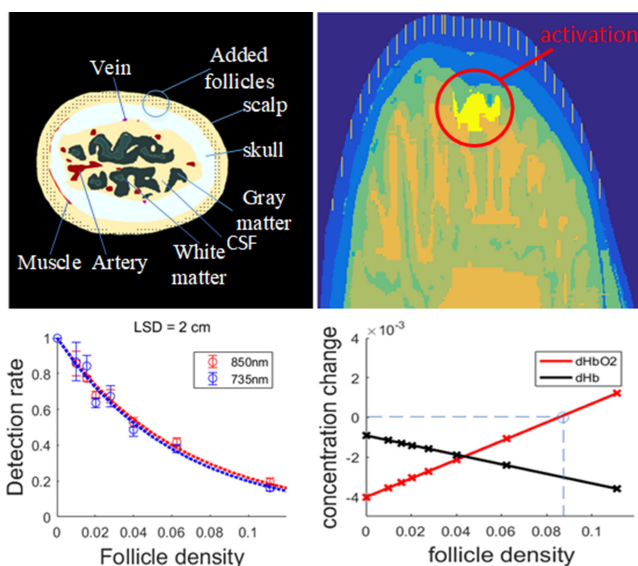
Xiang Fang
Boan Pan
Weichao Liu
Zhiyuan Wang
Ting Li

Effect of Scalp Hair Follicles on NIRS Quantification by Monte Carlo Simulation and Visible Chinese Human Dataset

Xiang Fang [1], **Boan Pan,**[2] **Weichao Liu,**[1] **Zhiyuan Wang,**[3] **and Ting Li** [1]

[1]Institute of Biomedical Engineering, Chinese Academy of Medical Science and Peking Union Medical College, Tianjin 300192, China
[2]State Key Laboratory Electronic Thin Film & Integrated Device, University of Electronic Science and Technology of China, Chengdu 610054, China
[3]School of Physics, Nankai University, Tianjin 370000, China

Abstract: Near-infrared spectroscopy (NIRS) has increasingly been used to noninvasively determine hemodynamic concentration change noninvasively by detecting light intensity changes. The effect of scalp hair follicle (SHF) on NIRS quantification is highlighted since its dark pigmentations is a strong absorption source to contaminate the NIRS signal. Here we have incorporated the Monte Carlo modeling for light transport in voxelized media, and visible Chinese human with high precision in depicting three-dimensional human anatomical structures, to study the effect of SHF density on NIRS quantification. The results quantified the strong impact of SHF on NIRS measurements and revealed that the detected light intensity signal decreased by 15%–80% when SHF density varied from 1% to 11.1% at Asian human range. More surprisingly, the hemodynamics-interpreted brain activation could be miscalculated by 11.7%–292.24% linearly with SHF density varied in 1%–11.1%. It is the first time that the effect of SHF on NIRS measurements has been quantitatively evaluated and the dramatic influence of SHF is outlined to be seriously concerned. The finding of the linear correlation between NIRS signal underestimation and the density of scalp hair follicles also indicate a potential calibration method to eliminate the SHF effect on NIRS measurement.

Index Terms: Scalp hair follicle, near-infrared spectroscopy (NIRS), Monte Carlo simulation, visible Chinese human (VCH).

1. Introduction

Near-infrared spectroscopy (NIRS) has been used to monitor concentration change of oxy-hemoglobin $\triangle[HbO_2]$ and deoxy-hemoglobin $\triangle[Hb]$ in the brain since 1977 and extended to investigate brain activity as functional near-infrared spectroscopy (fNIRS) by utilizing the theory of neurovascular coupling [1]. Since NIRS, including features such as non-invasion, portability, and lower susceptibility to motion artifacts, it has gained significant traction into wide range of

neuroscience applications including motor tasks [2], brain function evaluation [3], and neurological abnormality [4]. Furthermore, because of its safety and flexibility, fNIRS is well suited to the study of infants and children for language development, attention deficit hyperactivity disorder, and autism spectrum disorder [4].

The reliability of NIRS and fNIRS applications relies on the correct interpretation of fNIRS measurements. Over the last twenty years of development, multiple efforts to improve the accuracy of NIRS/fNIRS system have been made. These include source wavelength selection, source detector arrangement, and algorithm analysis, which have all been studied by various of groups [1]. However, there are still known factors whose effects cannot be fully eliminated. Strong absorption caused by dark pigmentations such as hair and hair follicle are considered to be one important source of interference [5], [6]. The effect of scalp hair and scalp hair follicle (SHF), which is common form of pigmentation, was considered during the study of probe design [7]. But few researches have discussed the effect of SHF quantitatively. Pringle *et al.* studied the effects of epidermal pigmentation and hair covering in large animals on near infrared light penetration with respect to differential pathlength factor [5], but no result corresponding to detected light intensity or hemodynamic concentration change was mentioned. Bilal Khan *et al.* developed brush optodes for fNIRS to improve the optical contact with scalp and avoid the obstruction by hair [8]. However, since the follicle tissue and part of the hair grows deep into scalp, light propagation through follicle tissue cannot be avoided, so the effect of follicles still exists.

Monte Carlo simulation is frequently used method to study light transportation in tissue. The most widely used model is based on layered tissue structure [9]. But the geometry of scalp hair follicles and the complicity of brain structure requires more sophisticated voxelized three-dimensional Monte Carlo tool to perform precise simulation. MCMV is a suitable simulation tools developed by our group [10]. Using a high resolution visible Chinese human corpse cryosection data set (VCH), it is feasible to study light propagation in the human head model with a precise head structure. This model was used to demonstrate penetration depth in the human brain for light propagation [11] and predict the existence of edema [12]. Here we use this method to analyze the effect of SHF with various distribution densities on light propagation in the accurate human head model, and quantitatively interpret the relationship between the follicle density and impact level on NIRS measurement.

Detected light intensity, brain activation induced detected intensity change, and calculated hemodynamic parameter change are all studied by the sequence of acquisition in the NIRS system. The simulation provided detected intensity with various densities and analyzed by Beer-Lambert law. Brain activation is simulated by manipulating the absorption coefficient in a designed activation zone to provide intensity change, which is further investigated by reformed definition equation. Hemodynamic concentration changes are then calculated by modified Beer-Lambert law (MBLL) with different SHF distribution densities and measuring the impact as demonstrated by the variation rate.

2. Methods

2.1 VCH Head and Follicle Model

Visible Chinese human(VCH) project provides several sets of computer tomographic, magnetic resonance and photographic images of normal adult male and female corpse [13]. We used the head of the photographic images of the adult male cryosection in this study. The original resolution of this set was 0.01 cm × 0.01 cm × 0.02 cm. For computational feasibility, we decrease the resolution to 0.04 cm × 0.04 cm × 0.04 cm during simulation. Pre-processing was done in the sequence of gray scaling, multiple threshold converting as shown in Fig. 1, to form the structure file used in the MCVM tool. A total of 7 tissue types were recognized, which are scalp, skull, muscle, cerebrospinal fluid (CSF), gray matter, white matter, artery, and vein.

Follicle structure are modeled by averaging the absorption and scattering coefficient of hair shaft with the area of follicle tissue according to the size ratio in planes parallel to scalp and stacked to certain depth in planes vertical to scalp. The size of one modeled follicle in x-z plane is 0.04 cm ×
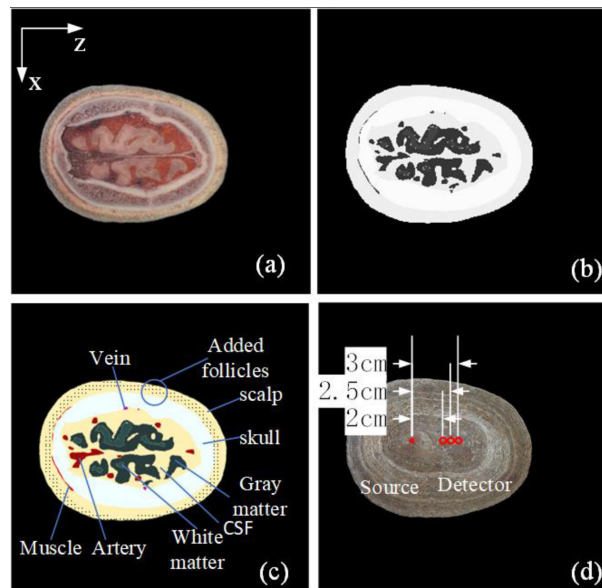
Fig. 1. VCH model and process procedure. (a) Original VCH model figure. (b) After gray scale process. (c) After multithresholds distinction process. (d) Arrangement of source and detectors.

TABLE 1

Optical Properties of Head Component at 850 nm/735 nm

Tissue type	$\mu_a\,(cm^{-1})$		$\mu_s\,(cm^{-1})$		g		n		Ref
	850nm	735nm	850nm	735nm	850nm	735nm	850nm	735nm	
Scalp	0.375	0.45	95	106	0.81	0.81	1.37	1.37	[15]
Skull	0.28	0.23	270	320	0.94	0.93	1.43	1.43	[16]
Muscle	0.295	0.388	66	78	0.90	0.90	1.40	1.40	[17]
CSF	0.0433	0.0158	0.1	0.1	0.90	0.90	1.33	1.33	[18]
Gray matter	0.35	0.2	85	74	0.90	0.90	1.37	1.37	[19]
White matter	1	0.8	370	360	0.87	0.855	1.37	1.37	[19]
Artery	6	0.6	290	300	0.99	0.99	1.4	1.4	[20]
Vein	0.31	0.8	290	300	0.99	0.99	1.4	1.4	[20]
hair follicle	1.78	2.06	700	900	0.95	0.95	1.57	1.57	[21, 22]

0.04 cm and the depth is no more than 0.4 cm. Voxelized follicles are added into the model layer by layer by substituting the scalp tissue index with the follicle index at assigned points. The assignation rule states that we substitute one pixel every 10, 8, 7, 6, 5, 4 or 3 pixels in each direction and only when the corresponding point is scalp within the first 100 layers. This kind of process leads to a series of follicle area to scalp area ratio (mentioned as follicle distribution density or follicle density in this article) of 1%, 1.56%, 2.05%, 2.78%, 4%, 6.25% and 11.11%, which is a reasonable range calculated from images in [14].

2.2 Monte Carlo Simulation Procedure

Head models with no follicle and 7 different follicle densities were used in the Monte Carlo simulation tool MCVM. The tissue structure files are sized as $498 \times 475 \times 150$ pixels. Each pixel is converted to one voxel in the simulation and results in the same resolution: 0.04 cm $\times$ 0.04 cm $\times$ 0.04 cm. The optical properties of each tissue type are collected from corresponding literatures and shown in Table 1 with references. The light source is defined as 0.1 cm radius Gaussian type and incidents
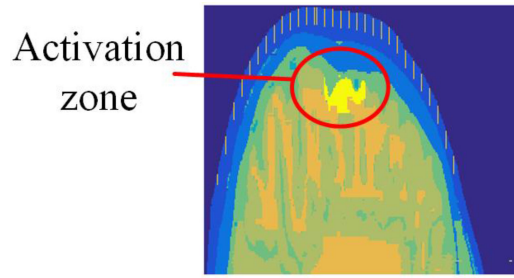
Fig. 2. Demonstration of the absorption coefficient change area.

vertically on vertex. Results of the specific position of incident light is shown in Fig. 1(d). We allowed 1×10^7 photon packages illuminating the head model for each simulation and simulation sets, which contains 5 simulations with same parameter, are used for each follicle density for two wavelengths for reflection intensity study. Two source-detector separation distances of 2 cm, 2.5 cm and 3 cm are used with a detector of 0.3 cm radius. The configurations are graphically shown in Fig. 1(d).

The event of local brain activation is simulated by running one additional simulation with verified tissue structure file, in which the absorption coefficient is doubled in a certain area for gray matter and for each density as shown in Fig. 2. Intensity change due to activation is calculated by using the result from one none activation simulation and one activation simulation with the same follicle density.

2.3 Data Analysis

The output files of MCVM provide information about the absorption distribution in the tissue and outflowing photon parameters including energy, position and direction. The absorption distribution file is used to form a signal sensitivity distribution (SSD) map using the same procedure as described in [23]. The outflowing photon intensity in the other file provided by MCVM simulation is calculated as the summation over time and specific area mentioned in Section 2.2. The pathlengths of each photon package traveled through every tissue type, and this was recorded in the same file. The weighted mean pathlength of each photon package was calculated for later analysis. According to Beer-Lambert law, the detected energy can be calculated as

$$w_D = w_I \exp\left(-\sum_{i=1}^{n} L_i \cdot \mu_{ai}\right) \tag{1}$$

where w is light intensity. The subscripts I and D denote input and detected. L_i and μ_{ai} are the pathlength and absorption coefficient for the corresponding tissue. Subscript i indicates the tissue type in the order of scalp, skull, muscle, artery, vein, CSF, gray matter, white matter and hair follicle. We further define w_0 as the detected intensity from no hair follicle structure simulation, w_n for intensity of certain density follicle case and detection rate A as the ratio of reflection intensity for certain follicle density case to the no follicle case. Therefore, the detection rate can be calculated as

$$A = \frac{w_n}{w_0} = \exp\left(-L_9 \mu_{a9} - \sum_{i=1}^{8} \Delta L_i \cdot \mu_{ai}\right). \tag{2}$$

Assuming pathlength photon traveled in follicle tissue is approximately linear to follicle density, and the first term in the bracket in equation (2) is significantly larger, then mathematically this ratio is approximately equivalent to an exponential decay function. Thus, for any measurement with certain follicle density ρ, the detected rate can be estimated as

$$A \approx \exp\left(-p \cdot \rho \cdot \mu_{a9}\right), \tag{3}$$

where p is a constant obtained from the fitting process. In addition to the detected intensity, the concentration change $\Delta[HbO_2]$ and $\Delta[Hb]$ may also be affected by the variation of follicle densities. Modified Beer-lambert law (MBLL) is usually used to calculate these two values by using the equation [24]

$$\Delta OD(\lambda) = \Delta\mu_a(\lambda)\,L l_{DPF}(\lambda) = \left[\varepsilon_{HbO_2}(\lambda)\,\Delta[HbO_2] + \varepsilon_{Hb}(\lambda)\,\Delta[Hb]\right]L l_{DPF}(\lambda), \qquad (4)$$

where $\Delta OD(\lambda)$ is the change in optical density measured at a given wavelength, $\Delta\mu_a(\lambda)$ is the corresponding change in absorption coefficient, L is the source detector separation, and $L_{DPF}(\lambda)$ is the differential pathlength factor (DPF). To analyze the effect of follicle on calculated concentration change, we first investigate the impact of detected intensity change since it is the parameter that is used to calculate concentration change. The intensity change can be written in the form

$$\Delta OD = -\log\frac{W_{an}}{W_n} = -\log\frac{W_{a0}}{W_0} - \log\frac{\frac{W_{an}}{W_{a0}}}{\frac{W_n}{W_0}}. \qquad (5)$$

From this equation, we can see that the first term on the right-hand side of equation (5) denotes the change in the case when no follicle exists while the second term indicates the influence of the follicle. We define the terms as $\Delta OD_{activation}$ and $\Delta OD_{follicle}$ respectively. The ratio of $\Delta OD_{follicle}$ to $\Delta OD_{activation}$ shows the quantitative level of the follicle effect to an activation event. The numerator and denominator in $\Delta OD_{follicle}$ represents two detection ratios with certain follicle density for activation and non-activation cases. By using the estimation of equation (3), the intensity change can be approximated by

$$\Delta OD \approx -\log\frac{W_{a0}}{W_0} - (p_n - p_a)\cdot\rho\cdot\mu_{a9}, \qquad (6)$$

Where p_n is the fitted coefficient for the non-activation case and p_a is the fitted coefficient for the activation case, and ρ is the density. As the first term is a constant from simulation result, the intensity change is estimated to a linear relation.

With the calculated intensity change in two different irradiation wavelengths, $\Delta[HbO_2]$ and $\Delta[Hb]$ can be calculated using equations (7), where ε is Extinction coefficients and $\varepsilon_{Hb}^{\lambda 1}$, $\varepsilon_{Hb}^{\lambda 2}$, $\varepsilon_{HbO2}^{\lambda 1}$ and $\varepsilon_{HbO2}^{\lambda 2}$ are chosen by the same manner as our previous work in [24].

$$\begin{pmatrix}\Delta[Hb]\\\Delta[HbO_2]\end{pmatrix} = \frac{1}{DPF\cdot L}\begin{pmatrix}\varepsilon_{Hb}^{\lambda 1} & \varepsilon_{HbO_2}^{\lambda 1}\\\varepsilon_{Hb}^{\lambda 2} & \varepsilon_{HbO_2}^{\lambda 2}\end{pmatrix}\begin{pmatrix}\Delta OD_{\lambda_1}\\\Delta OD_{\lambda_2}\end{pmatrix} \qquad (7)$$

To demonstrate the impact level of follicle on $\Delta[HbO_2]$ and $\Delta[Hb]$ quantitatively, variation rate R is calculated by equation (8), where X denotes $\Delta[HbO2]$ or $\Delta[Hb]$, n denotes the certain density case and 0 denotes the no follicle case.

$$R = \frac{X_n - X_0}{X_0} \qquad (8)$$

3. Results

SSD maps of follicle density 0%, 1% and 11.11% in two different planes are drawn in Fig. 3. The black contour lines indicate a sensitivity difference of 10 times. The contour line is severely distorted with increasing follicle density. It indicates that the light-fluence within the head is distorted, therefore, the detected intensity will also have variation.

The previously defined detection rate for different follicle densities for 2 cm, 2.5 cm and 3 cm source detector separation cases are simulated and the estimated exponential decay function is used to fit the tendency curve in Fig. 4. Circles show the average value from 5 simulations and error bars indicate the standard deviation. The dotted line is the assumed exponential decreasing tendency curve fitted from the mean ratios. The ratio of detected energy decreased to 20% exponentially with the linear increasing follicle density for both cases. When comparing the result from Fig 4.(a) and Fig 4.(b), two features can be seen. The first feature is that the standard deviation

Follicle density 11.11%   Follicle density 1%   No follicle
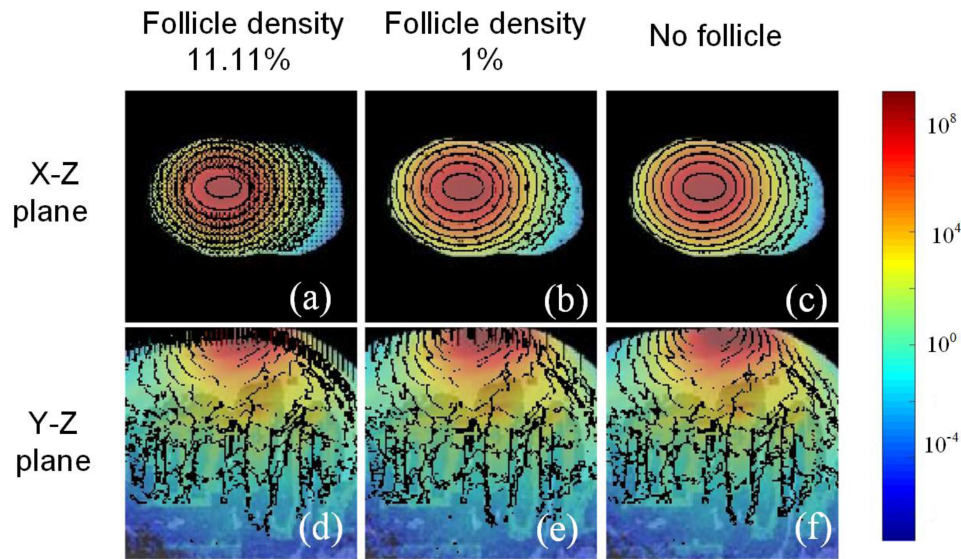
X-Z plane

Y-Z plane

Fig. 3. Signal sensitivity distribution (SSD) map with contour line for different follicle densities with source detector separation of 2 cm. (a) X-z plane view of follicle density 11.11% case; (b) x-z plane view of follicle density 1% case; (c) x-z plane view of no follicle case; (d) y-z plane view of follicle density 11.11% case; (e) y-z plane view of follicle density 1% case; (f) y-z plane view of no follicle case.
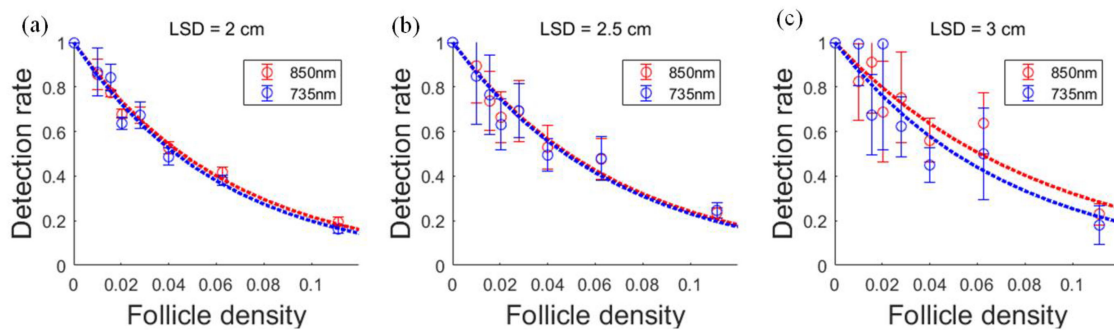
Fig. 4. Detection rate with variant follicle densities. (a) 2 cm S-D separation case; (b) 2.5 cm S-D separation case; (c) 3 cm S-D separation case, where circles represent average value of 5 simulation, error bars represent the standard deviation and dashed line presents the exponential fitting curve.

increases dramatically with source detector separation. The deviation from every simulation with same brain structure and follicle distribution may be caused by the statistic property inherent in the Monte Carlo simulation. When the separation is bigger, more incident photon packages are needed to cover all possibilities of scattering event, which sometimes are practically not feasible. The second feature is that the smaller the separation is, the smaller the estimation error will be. To evaluate the source of divergence, the assumption of the linear relation between follicle density and the light pathlength in follicle tissue will be experimentally verified.

The result in Fig. 5 experimentally demonstrates the validation of the linear relationship used in equation (3). When the source detector separation is 2 cm, R-square value and RMSE for linear fitting is 0.9935 and 0.01989 for 850 nm irradiation while these values are 0.9924 and 0.01992 for 735 nm irradiation. When the source detector separation is 2.5 cm, R-square value and RMSE for linear fitting is 0.9839 and 0.0055 for 850 nm irradiation while these values are 0.9694 and 0.006823 for 735 nm irradiation. When the separation increases to 3 cm, these values are 0.9836, 0.0262, 0.9883, and 0.0212 respectively. The linearity is not obviously violated according to R-square value
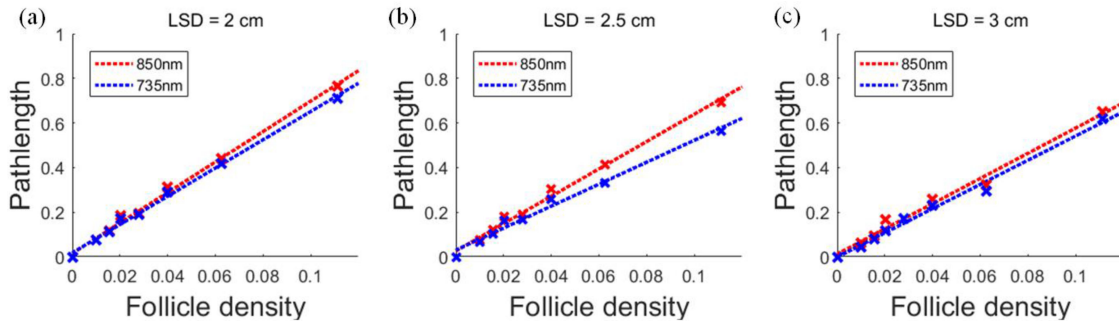
Fig. 5. Linear fitting for follicle density versus pathlength in follicle tissue. (a) 2 cm S-D separation case; (b) 2.5 cm S-D separation case; (c) 3 cm S-D separation case, where crosses represent the simulated value and dashed lines represent the linear fitting curves.
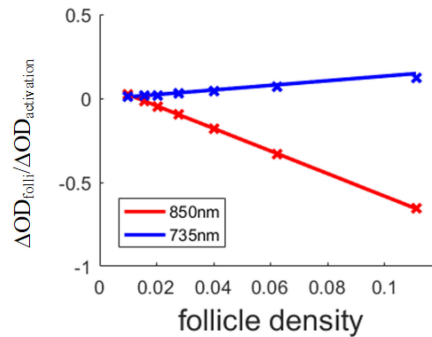

Fig. 6. Effect ratio of follicle to the result of detected intensity change in source detector separation 2 cm case, where crosses are calculated data points and the solid lines indicate the linear trend.
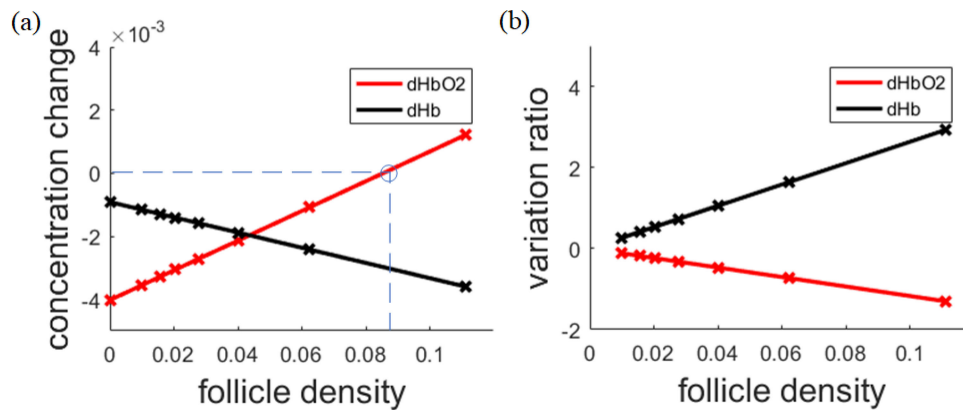

Fig. 7. Calculation result from MBLL. (a) Concentration change of HbO_2 and Hb, where crosses are the calculated points, solid lines represent the linear trends and the circle indicates the sign changing point for $\Delta[HbO_2]$; (b) concentration change variation ratio of HbO_2 and Hb according to equation (8), where crosses are the calculated points, solid lines represent the linear trends of variation ratio with follicle density.

when source-detector separation increases from 2 cm to 3 cm, which indicates that the estimation error is primarily caused by some other factor and will be discussed later.

The effect of follicles on detected intensity change when an area of gray matter is activated calculated by equation (6), is shown in Fig. 6. Previously defined ratio of $\Delta OD_{follicle}$ to $\Delta OD_{activation}$ provides an intuitive parameter to quantify the influence. More importantly, the term of $\Delta OD_{follicle}$

can be estimated by the two independent exponential estimation validated earlier in this paper. By dividing the estimated $\Delta OD_{follicle}$ by simulated $\Delta OD_{follicle}$, we found that the ratio changes from 2.25% to −65.65% in 850 nm irradiation case, while it increases from 0.86% to 14.77% in 735 nm case with linear follicle density growth. The minus ratio indicates that the change due to follicle is to the opposite direction to change due to activation.

The calculated hemodynamic changes for one certain activation event with different follicle densities according to equation (7) are displayed in Fig. 7(a) while the variation ratio comparing to the no follicle case are shown in Fig. 7(b). The calculated $\Delta[HbO_2]$ increases from −0.004 mmol/l to 0.0012 mmol/l while $\Delta[Hb]$ decrease from −0.0009 mmol/l to −0.0036 mmol/l when the follicle density increases from 0 to 11.11%. The variation ratio changes from 11.7% to −130.01% for $\Delta[HbO_2]$ and from 26.3% to 292.24% for $\Delta[Hb]$, which means increasing follicle density enhances the increasing absolute value of $\Delta[Hb]$ and enhances the decreasing absolute value of $\Delta[HbO_2]$. Furthermore, we observed that $\Delta[HbO_2]$ turns positive when the density increases to about 8.5%, which indicates that the effect of follicle may even change the sign of calculated hemodynamic parameter change.

4. Conclusion and Discussion

In this study, we investigated the effect of scalp hair follicle density variation on NIRS measurements by high-resolution cryosectional color photograph of a standing Chinese male adult and voxelized Monte Carlo simulation tool MCVM. Head models with different follicle distribution densities were made by manipulating the VCH dataset. The reflectance intensity was demonstrated to be approximately exponentially decreasing to 20% when follicle density increased to 11.11%. Detected intensity change, when activation in the brain occurs, was measured by a simulated part, which representing the influence from activation event, and another estimating part representing the influence of follicle. The result was used to calculate the hemodynamic concentration change. We found that the dense follicle distribution can disturb the calculated concentration change by nearly 292.24%, or even change the sign.

The exponential decaying tendency for reflection intensity within certain source detector separation indicates that there is a potential to quantitatively estimate the effect of follicle with various densities by limited numbers of simulation in advance. The implicit reason for the existence of the exponential relation may be the linear relationship between density and pathlength photons that travelled in follicle tissue area and the deduction from Beer-Lambert law. The variation between simulated detection rate and calculated detection rate by fitting is under 7.84% when follicle density increases to 11.11% for 2 cm separation and 850 nm irradiation case and under 23.6% for 3 cm separation case. The approximation becomes poorer when separation distance increases. This phenomenon may be partly due to the assumption that pathlength relation in equation (2) becomes weaker, and partly due to the Beer-Lambert law not considering signal sensitivity inhomogeneity, which is heavily distorted when follicle density is higher as shown in Fig. 3.

For the detected intensity change when activation happens, the separation of the two influences does not only provide a reasonable approach to quantify the impact of follicle, but also provides a potential method to estimate the effect level with different follicle density, when combined with the estimation method for reflection intensity. The denominator of $\Delta OD_{follicle}$ is actually what we studied in the detected intensity section. The numerator has the same form but only with activated brain as the optical background instead of non-activated brain. For our simulation study, it can also be estimated exactly the same way as the denominator, however, further study is needed.

The calculation for hemodynamic concentration change in this study is based on modified Beer-Lambert law which is mathematically formed as a linear computation utilizing detected intensity change and a matrix formed by extinction coefficient as denoted in equation (7). Since the detected intensity change can be estimated as a linear form to follicle density change, calculated $\Delta[HbO_2]$ and $\Delta[Hb]$ also variate linearly with it. Noticing that the activation term on detected intensity change may alter with position and level of activation, the calculated effect of follicle on

hemodynamic concentration change is only present for this specific activation situation and source detector arrangement, but the method can be easily adopted to any desired situations.

Besides the discussion of quantitative analysis, there are some limitations in the modeling and simulation process that needs to be mentioned. Our modeling method for follicle tissues is a compromise between the accuracy of VCH model and computational cost in simulation. Even though hair shaft in follicle contributes most of the disturbance, averaging the parameter according to area ratio may cause inaccuracy since dispersed optical property is not precisely equal to aggregating them in one big area as discussed in [25]. The optical property of our follicle model only focused on the Asian population which means the modulation of follicle optical properties is based on black and gray hair shaft. Follicle with lighter colored hair may have less effect than reported here.

To conclude, the presented study simulated the effect of scalp hair follicle with various densities on the detected intensity, detected intensity change when activation of a functional brain area occurs, and hemodynamic parameters change due to activation by VCH human corpse dataset and voxelized Monte Carlo simulation tool. The influence of SHF is significant. The finding of the linear correlation between NIRS measurement underestimation and the density of SHF also indicates a potential calibration method to eliminate the effect on NIRS measurement. The accuracy of using MBLL to calculate focal brain activation is not discussed here because it is out of the scope of the present study. Further work may include investigating the effect of SHF on hemodynamic measures by other algorithms such as spatially resolved NIRS, diffuse optical tomography [26], and diffuse correlation spectroscopy [27].

References

[1] F. Scholkmann *et al.*, "A review on continuous wave functional near-infrared spectroscopy and imaging instrumentation and methodology," *Neuroimage*, vol. 85, pp. 6–27, 2014.

[2] D. R. Leff *et al.*, "Assessment of the cerebral cortex during motor task behaviors in adults: A systematic review of functional near infrared spectroscopy (fNIRS) studies," *Neuroimage*, vol. 54, no. 4, pp. 2922–2936, 2011.

[3] A. Chaddad, "Brain function evaluation using enhanced fNIRS signals extraction," in *Proc. 48th Annu. Conf. Inf. Sci. Syst.*, 2015, pp. 1–4.

[4] H. Y. Kim, K. Seo, H. J. Jeon, U. Lee, and H. Lee, "Application of functional near-infrared spectroscopy to the study of brain function in humans and animal models," *Molecules & Cells*, vol. 40, no. 8, pp. 523–532, 2017.

[5] J. Pringle, C. Roberts, M. Kohl, and P. Lekeux, "Near infrared spectroscopy in large animals: Optical pathlength and influence of hair covering and epidermal pigmentation," *Veterinary J.*, vol. 158, no. 1, pp. 48–52, 1999.

[6] M. A. Mcintosh, U. Shahani, R. G. Boulton, and D. L. Mcculloch, "Absolute quantification of oxygenated hemoglobin within the visual cortex with functional near infrared spectroscopy (fNIRS)," *Investigative Ophthalmol. Vis. Sci.*, vol. 51, no. 9, pp. 4856–4860, 2010.

[7] G. Strangman, D. A. Boas, and J. P. Sutton, "Non-invasive neuroimaging using near-infrared light," *Biol. Psychiatry*, vol. 52, no. 7, pp. 679–693, 2002.

[8] B. Khan *et al.*, "Improving optical contact for functional near-infrared brain spectroscopy and imaging with brush optodes," *Biomed. Opt. Exp.*, vol. 3, no. 5, pp. 878–898, 2012.

[9] S. L. Jacques and L. Wang, "Monte Carlo Modeling of Light Transport in Tissues," *Comput. Methods Programs Biomed.*, vol. 47, no. 2, pp. 73–100, 1995.

[10] T. Li, H. Gong, and Q. Luo, "MCVM: Monte Carlo modeling of photonmigration in voxelized media," *J. Innovation Opt. Health Sci.*, vol. 3, no. 2, pp. 91–102, 2010.

[11] T. Li, C. Xue, P. Wang, Y. Li, and L. Wu, "Photon penetration depth in human brain for light stimulation and treatment: A realistic Monte Carlo simulation study," *J. Innovative Opt. Health Sci.*, vol. 10, no. 5, 2017, Art. no. 1743002.

[12] L. Wu, Y. Lin, and T. Li, "Effect of human brain edema on light propagation: A Monte Carlo modeling based on the visible chinese human dataset," *IEEE Photon. J.*, vol. 9, no. 5, Oct. 2017, Art. no. 6101810.

[13] S. X. Zhang *et al.*, "The Chinese Visible Human (CVH) datasets incorporate technical and imaging advances on earlier digital humans," *J. Anatomy*, vol. 204, no. 3, pp. 165–173, 2004.

[14] P. Yaprohm, J. Manonukul, V. Sontichai, J. Pooliam, and S. Srettabunjong, "Hair follicle counts in Thai population: A study on the vertex scalp area," *J. Med. Assoc. Thailand*, vol. 96, no. 12, pp. 1578–1582, 2013.

[15] A. N. Bashkatov, E. A. Genina, V. I. Kochubey, and V. V. Tuchin, "Optical properties of human skin, subcutaneous and mucous tissues in the wavelength range from 400 to 2000 nm," *J. Phys. D, Appl. Phys.*, vol. 38, no. 38, 2005, Art. no. 2543.

[16] M. Firbank, M. Hiraoka, M. Essenpreis, and D. T. Delpy, "Measurement of the optical properties of the skull in the wavelength range 650–950 nm," *Phys. Med. Biol.*, vol. 38, no. 4, pp. 503–510, 1993.

[17] S. L. Jacques, "Optical properties of biological tissues: a review," *Phys. Med. Biol.*, vol. 58, no. 11, pp. 37–61, 2013.

[18] G. M. Hale and M. R. Querry, "Optical constants of water in the 200-nm to 200-μm wavelength region," *Appl. Opt.*, vol. 12, no. 3, pp. 555–563, 1973.

[19] P. C. S. A N Yaroslavsky, I. V. Yaroslavsky, R. Schober, F. Ulrich, and H.-J. Schwarzmaier, "Optical properties of selected native and coagulated human brain tissues in vitro in the visible and near infrared spectral range," *Phys. Med. Biol.*, vol 47. no. 12, pp. 2059–2073, 2002.

[20] A. Roggan, M. Friebel, R. K. Do, A. Hahn, and L. G. Mu, "Optical Properties of circulating human blood in the wavelength range 400–2500 nm," *J. Biomed. Opt.*, vol. 4, no. 1, pp. 36–46, 1999.

[21] A. N. Bashkatov, E. A. Genina, G. B. Altshuler, and V. V. Tuchin, "Optical properties of hair shafts estimated using the digital video microscopic system and inverse Monte Carlo method," *Proc. SPIE*, vol. 4609, pp. 1–9, 2002.

[22] X. J. Wang, R. P. Dhond, W. V. Sorin, J. S. Nelson, S. A. Newton, and T. E. Milner, "Characterization of human scalp hairs by optical low-coherence reflectometry," *Opt. Lett.*, vol. 20, no. 6, pp. 524–526, 1995.

[23] T. Li, Y. Li, Y. Sun, M. Duan, and L. Peng, "Effect of head model on Monte Carlo modeling of spatial sensitivity distribution for functional near-infrared spectroscopy," *J. Innov. Opt. Health Sci.*, vol. 8, no. 05, 2015, Art. no. 1550024.

[24] Y. Zhao, L. Qiu, Y. Sun, C. Huang, and T. Li, "Optimal hemoglobin extinction coefficient data set for near-infrared spectroscopy," *Biomed. Opt. Exp.*, vol. 8, no. 11, pp. 5151–5159, 2017.

[25] S. L. Jacques, "Optical assessment of cutaneous blood volume depends on the vessel size distribution: A computer simulation study," *J. Biophoton.*, vol. 3, nos. 1/2, pp. 75–81, 2010.

[26] D. A. Boas, T. Gaudette, G. Strangman, X. Cheng, J. J. A. Marota, and J. B. Mandeville, "The accuracy of near infrared spectroscopy and imaging during focal changes in cerebral hemodynamics," *Neuroimage*, vol. 13, no. 1, pp. 76–90, 2001.

[27] T. Li *et al.*, "Simultaneous measurement of deep tissue blood flow and oxygenation using noncontact diffuse correlation spectroscopy flow-oximeter," *Sci. Rep.*, vol. 3, no. 1, 2013, Art. no. 1358.